J. Fluid Mech. (2010), *vol.* 659, *pp.* 24–42.
doi:10.1017/S0022112010002399

Patterns in rotating Rayleigh–Bénard convection at high rotation rates

J. D. SCHEEL[1]†, P. L. MUTYABA[2] AND T. KIMMEL[2]

[1]Department of Physics, Occidental College, 1600 Campus Road, M21, Los Angeles, CA 90041, USA

[2]Department of Physics, California Lutheran University, 3750, Thousand Oaks, CA 91360, USA

(Received 7 September 2009; revised 15 April 2010; accepted 16 April 2010;

We present the results from numerical and theoretical investigations of rotating Rayleigh–Bénard convection for relatively large dimensionless rotation rates, $170 < \Omega < 274$, and a Prandtl number of 6.4. Unexpected square patterns were found experimentally by Bajaj *et al.* (*Phys. Rev. Lett.*, vol. 81, 1998, p. 806) in this parameter regime and near threshold for instability in the bulk. These square patterns have not yet been understood theoretically. Sánchez-Álvarez *et al.* (*Phys. Rev. E*, vol. 72, 2005, p. 036307) have found square patterns in numerical simulations for similar parameters when only the Coriolis force is included. We performed detailed numerical studies of rotating Rayleigh–Bénard convection for the same parameters as the experiments and simulations. To better understand these patterns, we compared the effects of the Coriolis force as well as the centrifugal force. We also computed the coefficients of the amplitude equation describing one-, two- and three-mode bulk solutions to rotating Rayleigh–Bénard convection. We find that squares are unstable, but we do find stable limit cycles consisting of three coupled oscillating amplitudes, which can superficially resemble squares, since one of the three amplitudes is rather small.

Key words: Bénard convection, pattern formation

1. Introduction

One of the most productive systems for studying pattern formation is Rayleigh–Bénard convection, which, in addition to exhibiting stable roll states, also has spatiotemporally chaotic states. In Rayleigh–Bénard convection, a fluid cell bounded by parallel plates is kept at a constant temperature difference ΔT. This leads to a buoyancy-driven instability as ΔT increases past a critical value. In rotating convection, the entire cell is rotated rigidly about a vertical axis with a constant rotation rate Ω_D. Hence, the system no longer has reflection symmetry, but maintains rotational symmetry (Knobloch 1998). For large enough rotation rates, a chaotic state known as domain chaos (due to the Küppers–Lortz instability) has been found to exist (Küppers & Lortz 1969; Tu & Cross 1992). This state consists of domains of parallel rolls, each of whose particular location and size vary chaotically.

Unexpected square patterns were found experimentally by Bajaj *et al.* (1998) and Ahlers & Bajaj (1999), in this same parameter regime. These square patterns have not yet been understood theoretically. Sánchez-Álvarez *et al.* (2005) have found square patterns in numerical simulations for similar parameters when only the Coriolis force

---

† Email address for correspondence: jscheel@oxy.edu

is included, clearly indicating that the centrifugal force is not responsible for the patterns. A wall localized mode also exists in these finite cells, and previous studies are in disagreement as to whether this wall mode is responsible for the square patterns. For example, Marques & Lopez (2008) found a correlation between the mode number and the presence of square patterns in their simulations, suggesting that the wall mode strongly influences the bulk pattern. But, more recently, Rubio, Lopez & Marques (2010) found interior localized square patterns near onset for much lower rotation rates ($\Omega = 19.7$), but in a regime where the wall mode instability had not yet set in, suggesting that the wall mode may be unimportant.

Rotating Rayleigh–Bénard convection has been studied extensively for lower rotation rates both experimentally (Hu, Ecke & Ahlers 1995, 1997) and numerically for small aspect ratio periodic cells (Demircan, Scheel & Seehafer 2000; Demircan & Seehafer 2001) as well as larger aspect ratio (Scheel & Cross 2005; Rubio *et al.* 2010). Other than Sánchez-Álvarez *et al.* (2005) and Marques & Lopez (2008), rotating Rayleigh–Bénard convection has not been studied for higher rotation rates ($170 < \Omega < 274$), intermediate Prandtl number ($\sigma = 6.4$) and experimentally realistic finite boundary conditions. Rotating Rayleigh–Bénard convection has been studied at these rotation rates for annular channels, both with curvature (Scheel *et al.* 2003) and with infinite curvature (Chang, Liao & Zhang 2006; Zhan *et al.* 2009). In these cases, the counter-propagating travelling wall modes are the first to set in, and then a domain chaos state develops in the bulk as a secondary instability. For even higher Rayleigh numbers, the bulk becomes disorganized. For the annular channels studied, square patterns were always found to be unstable, although they did sometimes appear as transient states.

Finally, theoretical predictions have been made for roll, square and hexagonal planforms (Goldstein, Knobloch & Silber 1990, 1992). It has been known for a long time that squares are always unstable (Cross & Greenside 2009) in rotating Rayleigh–Bénard convection. In addition, theoretical work (Zhang & Liao 2008) has been done on computing asymptotic solutions (for $\Omega = 1000$) for arbitrary Prandtl number and aspect ratio, but assuming the existence of only a single azimuthal mode. The threshold for convection is defined as when convection sets in, either in the bulk or as a wall mode, and their solutions agree well with simulations. However, theoretical work by Rubio *et al.* (2010) for lower rotation rates ($\Omega = 20$) indicates that several distinct azimuthal modes set in with similar growth rates near onset, making this type of asymptotic approach problematic for lower rotation rates.

In this paper, we study the rotation rate regime ($170 < \Omega < 274$) where the origin of the square patterns remains a mystery. The effects of the centrifugal as well as the Coriolis force are included. We find that there is better side-by-side agreement with experiments when we include the centrifugal force, although the qualitative results agree even when the centrifugal force is neglected, at least for low enough rotation rates and near threshold. We also study the influence of the wall mode on the bulk, and find the persistence of ‘square-like’ patterns even when there is no wall mode, as in a periodic geometry. Finally, we compute the coefficients of the one, two and three coupled amplitude equations for Rayleigh–Bénard convection in the bulk with no-slip boundary conditions and the inclusion of the Coriolis force. We find that squares are always unstable, but there are Hopf bifurcations to oscillatory three-mode amplitude equation solutions which can superficially resemble squares. Upon a closer investigation, we find good agreement between our simulations and these amplitude equation solutions near threshold.

2. Boussinesq equations

The system is modelled by the Boussinesq equations augmented by the Coriolis force and the centrifugal force (Becker *et al.* 2006). The variables are non-dimensionalized by specifying the length in terms of the cell height d, the temperature in terms of ΔT and the time in units of the vertical thermal diffusion time $\tau_v = d^2/\kappa$, where κ is the thermal diffusivity. The equations are

$$\sigma^{-1}(\partial_t + \boldsymbol{u}\cdot\nabla)\boldsymbol{u} = -\nabla P + \nabla^2\boldsymbol{u} + \theta\hat{z} + 2\Omega\boldsymbol{u}\times\hat{z} - \frac{\beta\sigma\Omega^2}{R_c}\theta\boldsymbol{r}, \tag{2.1}$$

$$(\partial_t + \boldsymbol{u}\cdot\nabla)\theta = \nabla^2\theta + Rw, \tag{2.2}$$

$$\nabla\cdot\boldsymbol{u} = 0. \tag{2.3}$$

The variable $\boldsymbol{u}(\boldsymbol{r}, t) \equiv (u, v, w)$ is the velocity field, $P(\boldsymbol{r}, t)$ is the pressure, and $\theta(\boldsymbol{r}, t)$ is the temperature deviation from the linear conduction profile. The symbol ∂_t indicates time differentiation, and $\hat{z}$ is a unit vector in the vertical direction. The Prandtl number $\sigma = \nu/\kappa$, where ν is the kinematic viscosity. The Rayleigh number $R = \alpha g \Delta T d^3/\kappa\nu$, where α is the thermal expansion coefficient and g is the acceleration of gravity. The variable Ω is the dimensionless rotation rate ($\Omega = \Omega_D d^2/\nu$). The aspect ratio Γ is defined for square cells as the ratio of the length of the cell to its depth d and for cylindrical cells as the ratio of the radius to the depth. The variable $\beta = \alpha\Delta T_c$, and ΔT_c (and corresponding critical Rayleigh number R_c) is the temperature difference at which conduction gives way to convection.

Our boundary conditions along the top and bottom plates are no-slip and conducting:

$$u = v = w = \theta = 0 \quad \text{at} \quad z = 0, 1. \tag{2.4}$$

For realistic boundary conditions on the sidewalls, we use no-slip velocity boundary conditions and conducting or insulating thermal boundaries:

$$\begin{gathered}\text{Conducting boundaries}\\ \boldsymbol{u} = 0,\ \theta = 0 \quad \text{at} \quad r = \Gamma,\end{gathered} \tag{2.5}$$

$$\begin{gathered}\text{Insulating boundaries}\\ \boldsymbol{u} = 0,\ \frac{\partial\theta}{\partial r} = 0 \quad \text{at} \quad r = \Gamma.\end{gathered} \tag{2.6}$$

We also used periodic (for square regions only, of course) boundary conditions on the sidewalls:

$$\begin{gathered}\text{Periodic boundaries}\\ \boldsymbol{u}(x+\Gamma, y) = \boldsymbol{u}(x, y), \quad \theta(x+\Gamma, y) = \theta(x, y), \quad \text{and}\\ \boldsymbol{u}(x, y+\Gamma) = \boldsymbol{u}(x, y), \quad \theta(x, y+\Gamma) = \theta(x, y).\end{gathered} \tag{2.7}$$

For all our runs and calculations, we used a Prandtl number of 6.4, cylindrical aspect ratio $\Gamma = 5$ and square aspect ratio $\Gamma = 10$. We used a rotation rate $\Omega = 274$ to compare to the numerical results, $\Omega = 170$ to compare with the experiments, and also an intermediate $\Omega = 200$.

When including the centrifugal force, one needs to put in the parameters of a specific system, and we used parameters from the experiments (Bajaj *et al.* 1998). The two parameters necessary are (i) the depth of the cells (7.9 mm) and (ii) a value of the thermal diffusivity κ (1.5×10^{-7} m^2 s^{-1}). This yields a vertical diffusion time of 420 s.

With these numbers, we obtain Froude numbers $F = \Omega^2\sigma^2 d\Gamma/g\tau_v^2 = 0.03$ and 0.07 for the rotation rates of 170 and 274, respectively. This is at the lower limit of moderate Froude numbers according to Marques *et al.* (2007). Even in this regime, Marques *et al.* have found quantitative and qualitative changes in the flow dynamics. Likewise, Rubio *et al.* (2010) found qualitative differences for Froude numbers as low as 0.01. We find similar results, which are discussed below.

To solve the Boussinesq equations with rotation, we used the code Nek5000 (Fischer 1997) a parallel, spectral element code developed to solve the Navier–Stokes equation. This code is now readily available (https://nek5000.mcs.anl.gov/) and more than two dozen research institutions are using it. We used a time resolution of $0.0002\tau_v$. The spatial resolution corresponded to 11 (Gauss–Lobatto–Legendre) interpolation points per element dimension (so $11\times11\times11$ points per element), and an element side is equal to the depth of the cell. This translates to about 0.1 the depth of the cell, but there are more interpolation points near the boundaries than in the centre of each element, so the resolution changes from 0.02 (near the sides) to 0.15 (near the centre). The numerical code has been thoroughly checked (Chiam *et al.* 2003; Paul, Cross & Fischer 2002; Scheel *et al.* 2003; Scheel & Cross 2005; Becker *et al.* 2006; Scheel 2006, 2007) for these systems. We performed multiple runs for the systems described here, but with finer resolution ($11\rightarrow13\rightarrow15$ interpolation points) and found very similar results, with oscillation frequencies varying by at most 10 % as the resolution changed.

We varied our initial conditions between random values, parallel rolls and squares. As discussed below, the evolution of the dynamics strongly depended on the initial conditions.

3. Results

3.1. *Modulated trimodal patterns*

Table 1 summarizes our results, in which we varied the rotation rate, $\epsilon = (R - R_c)/R_c$, inclusion of centrifugal force, boundary conditions and initial conditions to cover a wide range of parameters.

The most clean example of a modulated trimodal pattern can be observed for the following case: $\Gamma = 5$, $\sigma = 6.4$, $\epsilon = 0.03$, $\Omega = 200$ and insulating boundary conditions as shown in the angle–time plot in figure 1(a). A snapshot of the pattern is shown in figure 2. The main modes rotate slightly in the prograde direction, as indicated by the tilt in figure 1(a). This is due to the finite size of the cell, and this angular velocity was measured by Sánchez-Álvarez *et al.* (2005) and is found to decrease as Γ increases. We also see this (compare figure 1a with figure 11). From figure 1(a) we measured a drift of about 700 vertical diffusion times for one full cycle, corresponding to an angular frequency of $2\pi/700 = 0.009$ rad τ_v^{-1}.

The amplitudes of the two modes which make up the ‘squares’ oscillate, and a third, weaker mode is also present, as can be more clearly seen in figure 1(b), which only shows the region from 650 to 800 vertical diffusion times. Note that this type of oscillation was also seen by Sánchez-Álvarez *et al.* (2005), although they only looked at the two orthogonal modes. This leads us to conclude that the ‘square’ pattern here is actually a modulated three-mode limit cycle to be discussed in § 3.4. We will call it a modulated trimodal pattern (MT) to distinguish it from the Küppers–Lortz (KL) pattern that can also be present. See the discussion just below (3.12) for an explanation of the KL instability.

To obtain this state, we started with an initial condition of squares (it is very difficult to find this state when starting from random conditions), and one sees that even

Ω	ϵ	Centrifugal force	Bulk pattern	m	k	Boundary conditions	Initial conditions
274	0.02	No	MT	38	8.7	cond	rand
274	0.05	No	MT	38	8.4–8.7	cond	rand
274	0.02	Yes	noisy	34	8.5	cond	rand
274	0.05	Yes	KL	34	8.5	cond	rand
200	0.03	No	MT	24	7.8	ins	squares
170	0.09	No	KL	32	7.3	cond	rand
170	0.09	Yes	KL	32	–	cond	par+rand
170	0.09	Yes	MT/KL	24	7.2	ins	rand
170	0.09	No	KL	26	7.3	ins	rand
170	0.09	Yes	MT/KL	24	7.2	ins	squares
170	0.09	No	KL	26	7.2	ins	squares

TABLE 1. A summary of the various patterns present for the aspect ratio $\Gamma = 5$, different rotation rates Ω and ϵ values. All of the simulations were for a Prandtl number of 6.4. The Coriolis force is always included, but the centrifugal force is only sometimes included, as noted. The pattern in the bulk is noted (KL = Küppers–Lortz pattern, MT = modulated trimodal). In addition, the mode number m of the wall mode was measured and is noted, as is the wavenumber of the bulk pattern, k. The boundary conditions ('cond' = conducting and 'ins'= insulating) and initial conditions ('rand' = random, 'par' = parallel rolls and 'squares' = two sets of rolls of equal amplitude and orthogonal orientation) are also noted. Note that for rotation rates of (170, 200, 274) the critical Rayleigh numbers are (18249, 22255, 32932).

though the usual KL pattern rapidly develops, the MT pattern coexists, and persists for a long time, even when the KL pattern has damped out completely (after $t = 300\tau_\nu$).

By taking Fourier transform of the temperature profile at midplane, we can extract the amplitude of the three dominant, straight, parallel modes A_1, A_2 and A_3. By looking at the sequence of events, $A_1 \rightarrow A_2$ corresponds to a switch of about $\pi/6$ rad, $A_2 \rightarrow A_3$ corresponds to a switch of about $\pi/3$ rad, and $A_3 \rightarrow A_1$ corresponds to a switch of $\pi/2$ rad. (A more careful investigation of the switching indicates the precise angles are $33\pi/180$, $57\pi/180$, $\pi/2$, but we have rounded here for simplicity.) The three modes are plotted as a function of time in figure 3. One can see that the system switches very cleanly and periodically among the three modes, with a period of 8.4 τ_ν per cycle which corresponds to an oscillation frequency of 0.75 rad τ_ν^{-1}. The amplitude of A_2 is significantly smaller than that of either A_1 or A_3, causing this MT state to superficially resemble squares.

3.2. *Comparisons to experiments and other simulations*

When we conducted our simulations with the same parameters as Sánchez-Álvarez *et al.* (2005), ($\Gamma = 5$, $\Omega = 274$, $\sigma = 6.4$, $\epsilon = 0.02$, and conducting thermal boundary conditions), we also saw the same type of 'square-like' pattern as shown in figure 4(a) and corresponding angle–time plot in figure 5(a). Although not very visible in figure 5(a), a very faint third mode is also present, so we will again denote this as an MT pattern. When we ran this simulation for a much longer time (but different, random initial conditions) as shown in figure 6, we do see a mixed MT/KL pattern. We also ran simulations for the same parameters as Sánchez-Álvarez *et al.* (2005), but included the centrifugal force as well. A snapshot is shown in figure 4(b) and the corresponding angle–time plot is shown in figure 5(b). The pattern here is extremely noisy and disorganized. It appears that the centrifugal force is strong enough for these rotation rates to disrupt the MT patterns. Note that the Froude

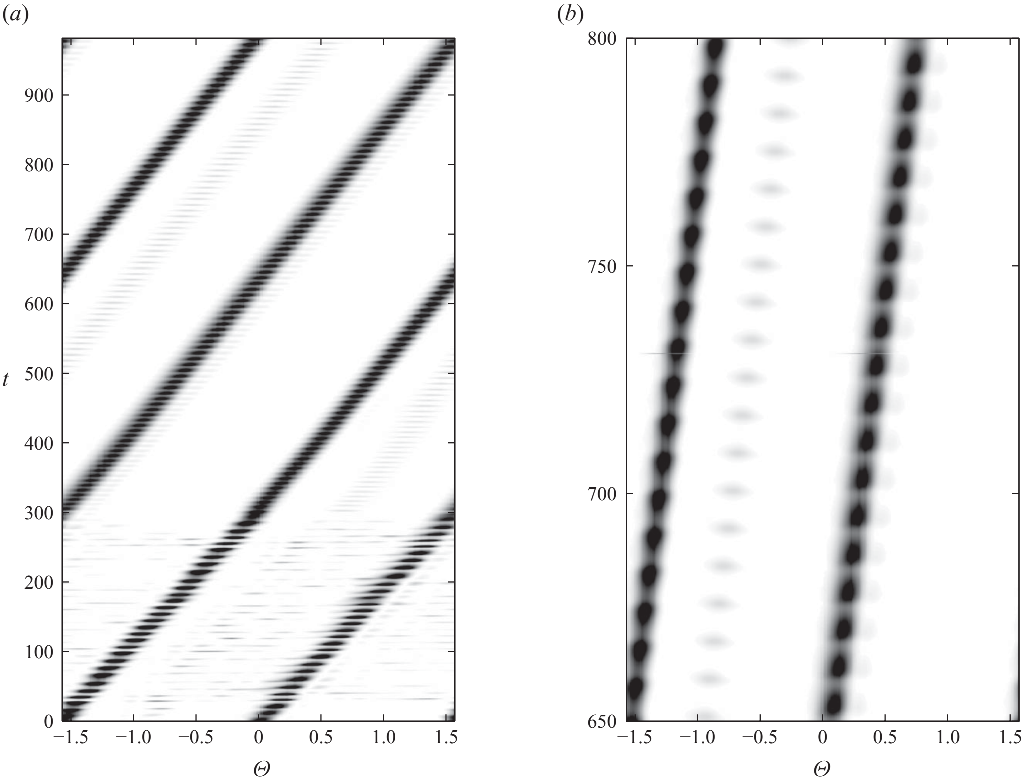

FIGURE 1. Angle–time plot for $\Gamma = 5, \sigma = 6.4$, $\epsilon = 0.03$, $\Omega = 200$, and insulating thermal boundary conditions. This is a density plot of the radially averaged Fourier power, $F(\Theta, t)$, as a function of orientation angle Θ and time t. Black corresponds to the largest value and white to the smallest. Because the angle of the rolls is a director field, only angles from $-\pi/2$ to $\pi/2$ are shown. Note that $-\pi/2$ maps onto $\pi/2$. (a) Entire time series shown. (b) Close-up of the region from 650 to 800 τ_v. The oscillation frequency is 0.75 rad τ_v^{-1}.

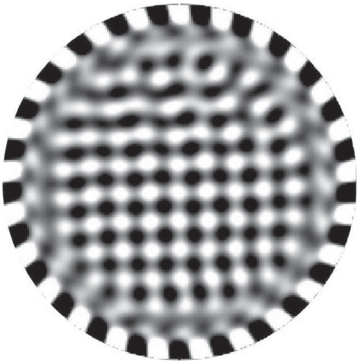

FIGURE 2. Snapshot of the temperature deviation θ at the midplane, for the same parameters as in figure 1. The grey denotes the conduction value ($\theta = 0$), and the lighter and darker shades give the values above and below this. The time is $650\,\tau_v$.

number is 0.07 here. We were unable to find MT patterns with the centrifugal force included at a rotation rate of 274.

We did, however, find MT patterns with the centrifugal force included when we ran the simulations at the lower rotation rate of 170 (and Froude number = 0.03),

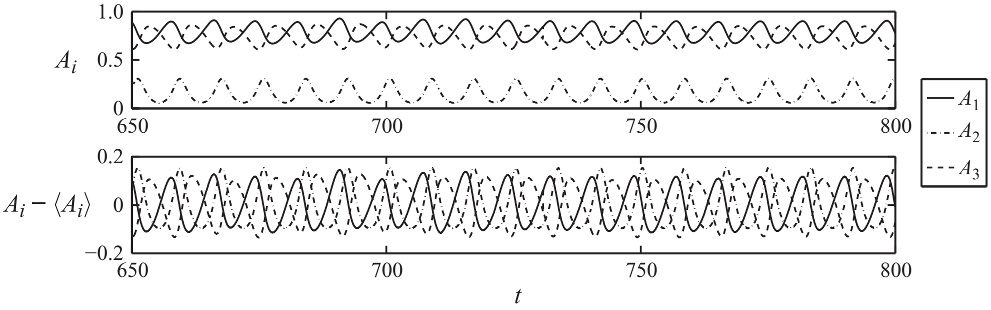

FIGURE 3. A plot of the amplitude versus time for the same parameters as in figure 1. The amplitude A_1 corresponding to rolls at $-\pi/2$ rad at 650 τ_v is the solid line, the amplitude A_2 corresponding to rolls at $-\pi/3$ rad at 650 τ_v is dash-dotted line and the amplitude A_3 corresponding to rolls at 0 rad at 650 τ_v is dashed. In the second plot, the means of the respective amplitudes are subtracted $A_i - \langle A_i \rangle$ so that the oscillations can be compared. The means are 0.78, 0.16 and 0.74, respectively.

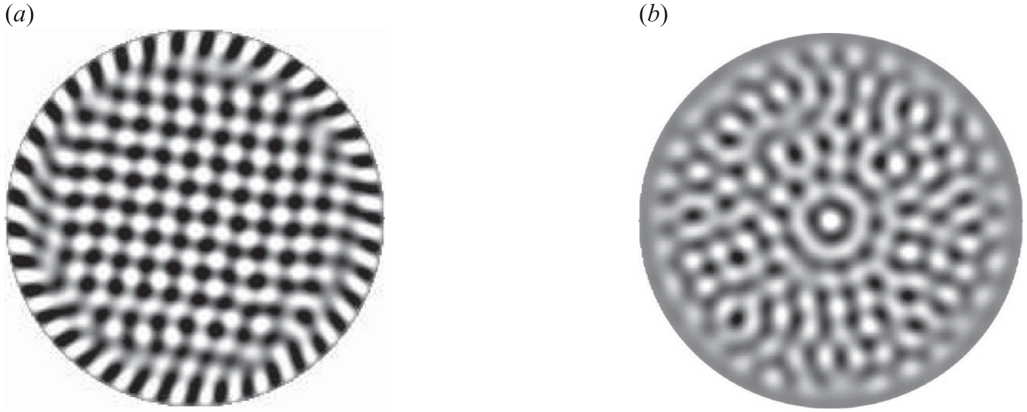

FIGURE 4. Snapshot of the temperature deviation θ at the midplane, for $\Gamma = 5$, $\sigma = 6.4$, $\epsilon = 0.02$ and $\Omega = 274$. Lateral temperature boundary conditions are conducting and random initial conditions were used. (a) Coriolis force only, $t = 33\,\tau_v$. (b) Centrifugal and Coriolis forces are included, $t = 6.22\,\tau_v$.

corresponding to the parameters used in the experiments by Bajaj *et al.* (1998). As seen in figure 7(b), an initial, possibly transient pattern of pure squares was found when we ran the simulations with the same parameters as the experiments. Eventually, these square patterns broke up, and a mixed MT/KL pattern developed instead as can be seen in the angle–time plot in figure 8(b).

We also ran the system in figure 7(b) for a much longer time, but this time with squares as the initial conditions. A typical snapshot is shown in figure 9 and the corresponding angle–time plot is shown in figure 10. This time we found the MT pattern to be intermittent with the KL state. This type of intermittency was also seen by Bajaj *et al.* (1998) in the experiments.

When we ran our simulations using only the Coriolis force, we were unable to find MT patterns for these parameters. A typical plot is shown in figure 7(a), and the corresponding angle–time plot is shown in figure 8(a).

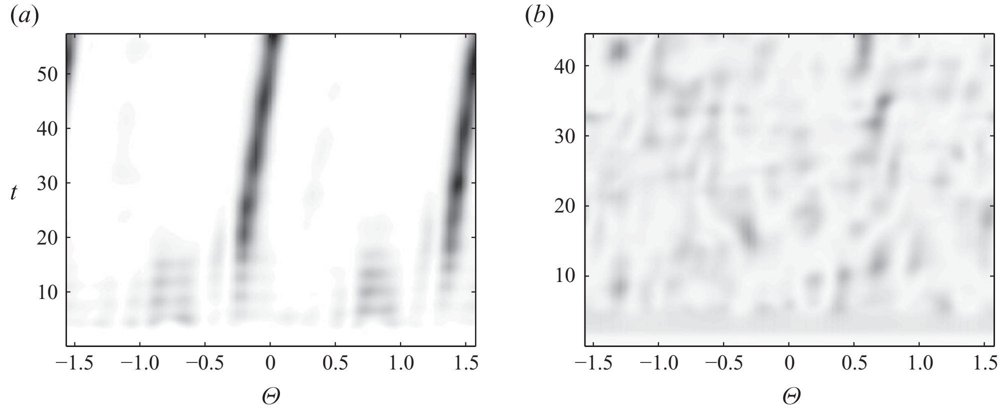

FIGURE 5. Angle–time plot for the same parameters as in figure 4. (*a*) Coriolis force only, oscillation frequency of 0.63 rad τ_ν^{-1}. (*b*) Centrifugal and Coriolis forces are included, with no discernible oscillation frequency.

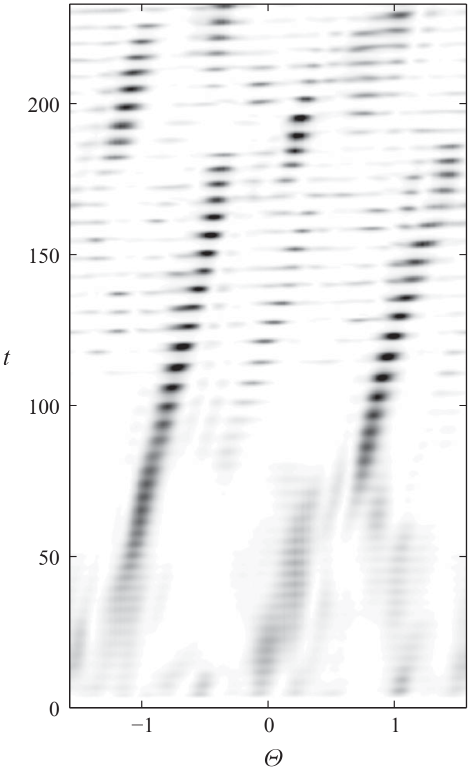

FIGURE 6. Angle–time plot for the same parameters as in figure 4(*a*) but for different random initial conditions. The oscillation frequency is 1.1 rad τ_ν^{-1}.

To summarize, we find MT, KL and mixed MT/KL patterns for a broad range of parameters, both with and without the inclusion of the centrifugal force. However, for a side-by-side exact comparison with experiments (for example, Bajaj *et al.* 1998), the centrifugal force needs to be included.

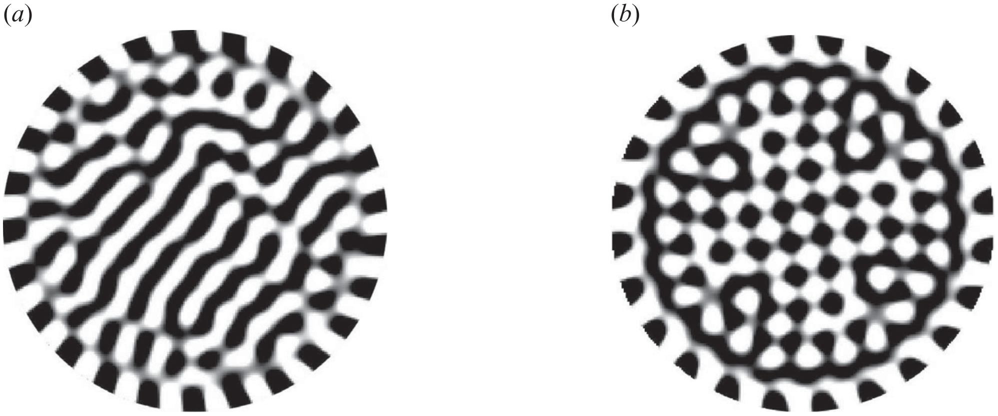

FIGURE 7. Snapshot of the temperature deviation θ at the midplane, for $\Gamma = 5$, $\sigma = 6.4$, $\epsilon = 0.09$ and $\Omega = 170$. Lateral temperature boundary conditions are insulating and random initial conditions were used. (*a*) Coriolis force only, $t = 8\,\tau_v$. (*b*) Centrifugal and Coriolis forces are included, $t = 11\,\tau_v$.

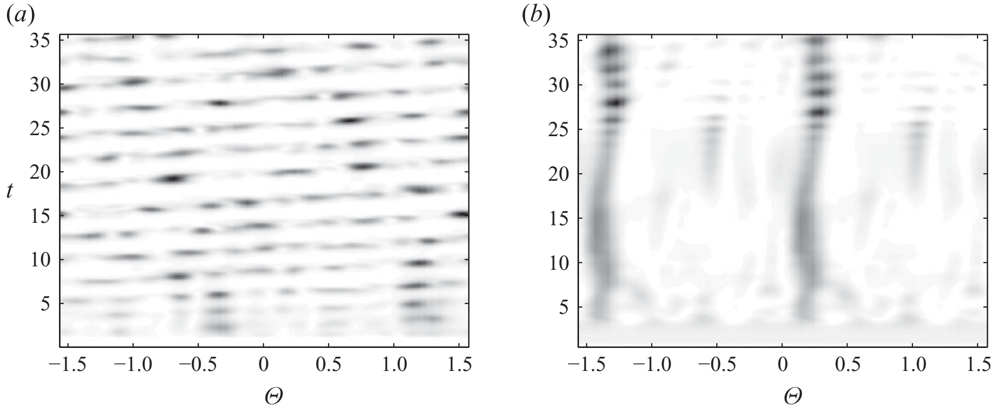

FIGURE 8. Angle–time plot for the same parameters as in figure 7. (*a*) Only the Coriolis force is included. The oscillation frequency is 2.2 rad τ_ν^{-1}. (*b*) The centrifugal force is also included. The oscillation frequency (after $t = 25\,\tau_\nu$) is 3.11 rad τ_ν^{-1}.

3.3. *Influence of wall mode on the bulk*

To determine if the wall mode influences the MT patterns, we also ran our simulations with periodic boundaries (2.7) for aspect ratio $\Gamma = 10$. As shown in figure 11, we see that the MT pattern does appear intermittently throughout the simulation, especially around 200 and then again around 300 vertical diffusion times. This suggests that these patterns are the result of a bulk pattern solution to (2.1)–(2.3) for rotating Rayleigh–Bénard convection with the inclusion of the Coriolis force. This is consistent with the results of Rubio *et al.* (2010), who found ‘square-like’ patterns very near threshold in cylindrical cells for $\Gamma = 11.8$, $\sigma = 4.5$, $\Omega = 19.7$, and with experimentally realistic boundary conditions. Since the rotation rate is so small for this case, the instability in the bulk sets in before the wall mode instability. This is further evidence that the MT patterns are independent of the wall mode and can exist without it.

Marques & Lopez (2008) studied the influence of the wall modes on the bulk for higher rotation rates ($\Omega = 625$), and did find a loose correlation between the

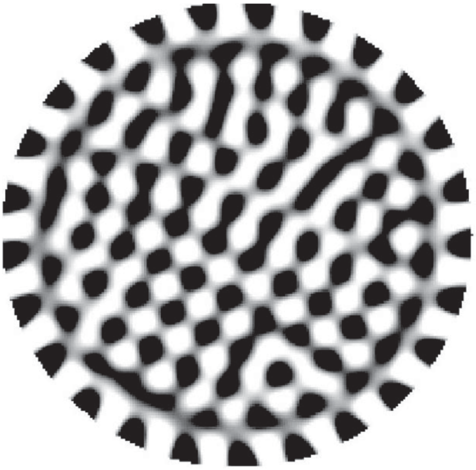

FIGURE 9. Snapshot of the temperature deviation θ at the midplane, for the same parameters as figure 8(*b*) except that the initial conditions were squares. The time is $74.7\,\tau_v$.

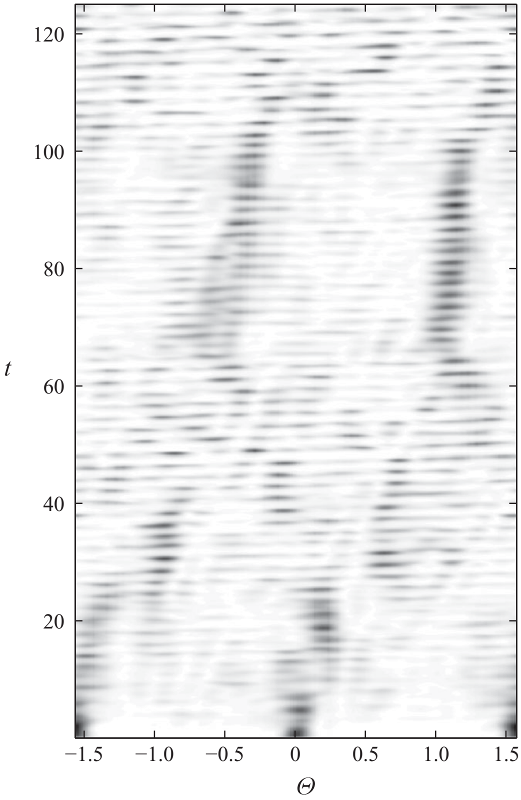

FIGURE 10. Angle–time plot for the same parameters as in figure 9. The oscillation frequency is 3.14 rad τ_v^{-1}.

wavenumber of the wall mode and the bulk pattern. They found 'square' patterns for a lower mode number and KL patterns for a higher mode number. We see no such correlation in our data (see table 1). For $\Omega = 274$, we see MT patterns for a higher mode number ($m = 38$) than the KL pattern ($m = 34$) and for $\Omega = 170$ the MT

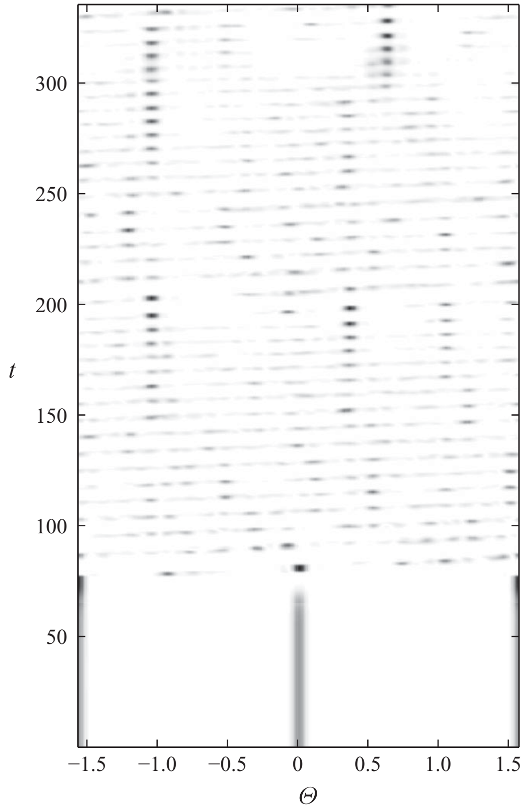

FIGURE 11. Angle–time plot for $\Gamma = 10, \sigma = 6.4$, $\epsilon = 0.02$ and $\Omega = 274$. Lateral temperature boundary conditions are periodic and the initial conditions are squares. The oscillation frequency is 1.0 rad τ_ν^{-1}.

patterns exist for a lower mode number ($m = 24$) than the KL pattern. However, note that the different boundary conditions for these two cases may also play a role here.

Our results clearly indicate that the wall mode does not influence the bulk for our parameters. Our own experience working with the wall mode in an annular geometry (Scheel *et al.* 2003) also suggests that the influence of the wall mode is only felt very near the walls. For annular regions it is useful to define $\delta r = r_0 - r_i$ as the difference between the outer and inner radii. We found that even for $\delta r = 0.5$, the counter-propagating wall modes on the inner and outer radii did not interfere with each other. This is consistent with Zhan *et al.* (2009), who found the inner and outer waves interacted for $\delta r \simeq\ < 0.375$. Zhan *et al.* (2009) suggested that the wall mode profoundly influences the bulk, since the dynamics is different for an annular channel where $\delta r = 2$ and $\Gamma = \infty$ and a square periodic cell with $\Gamma = 2$. However, an infinite annulus with $\delta r = 2$, $\Gamma = \infty$ is not equivalent to a periodic cell with $\Gamma = 2$. There is a different pattern of mean flow due to the presence of sidewalls in the former case (Scheel *et al.* 2003), which may have a stronger influence on the bulk than the wall mode, especially in larger aspect ratio systems. Also, as seen in Scheel *et al.* (2003), the net mean flow in annular cells decreases with increasing aspect ratio and decreasing ϵ. In conclusion, very near threshold and at $\Gamma = 5$, the bulk may be well described by the amplitude equation, even if a wall mode is present. The good agreement in table 2 suggests that this is indeed the case and the MT solutions to the amplitude equation

Ω	ϵ	ω (num)	$\omega(\pi/6, \pi/3, \pi/2)$	$\omega(\pi/3, \pi/6, \pi/2)$	$\omega(\pi/4, \pi/4, \pi/2)$	$\omega(\pi/3, \pi/3, \pi/3)$
170	0.090	2.2	2.4	1.0	1.9	6.5
200	0.027	0.75	0.8	0.25	0.6	2.25
274	0.022	1.0	0.8	0.0	0.55	2.35

TABLE 2. Oscillation frequency ω (num) in units of rad τ_v^{-1} for various parameters computed from the angle–time plots in comparison with the imaginary part of the complex eigenvalues for the four trimodal states. We used the data from figure 15 and multiplied by the respective ϵ values to obtain ω. The numerical values were found from figures 8, 1(*a*) and 11, respectively. (We always used cases where only the Coriolis force was included.)

provide an explanation for the 'square-like' patterns seen by Bajaj *et al.* (1998) and Sánchez-Álvarez *et al.* (2005).

3.4. *Amplitude equation analysis*

Following the same method as in Scheel (2007), we perform a multiple-scales analysis of the Boussinesq equations (2.1)–(2.3) with the Coriolis force for no-slip boundary conditions. We also neglect mean flow, since we will truncate our analysis at order $\epsilon^{3/2}$. As a result, a potential formulation (Scheel 2006) will suffice. We neglect the centrifugal force since the toroidal–poloidal decomposition (3.1) cannot accommodate the radial dependence.

Following Küppers & Lortz (1969) and Schlüter *et al.* (1965), we can decompose the velocity (u, v, w) into two arbitrary functions: ϕ, ψ:

$$\left.\begin{aligned} u &= \partial_z \partial_x \phi - \partial_y \psi, \\ v &= \partial_z \partial_y \phi + \partial_x \psi, \\ w &= -\left(\partial_x^2 + \partial_y^2\right)\phi, \end{aligned}\right\} \tag{3.1}$$

which is analogous to a toroidal–poloidal decomposition but makes the linear operator (see below) self-adjoint.

After various simplifications (Scheel 2006), (2.1)–(2.3) can be rewritten as

$$LV = N, \tag{3.2}$$

where L is the linear part of the Boussinesq equations, N is the nonlinear part, and

$$V = \begin{bmatrix} \phi \\ \psi \\ \theta \end{bmatrix}. \tag{3.3}$$

We will separate out fast (x, z) and slow (X, Y, T) scales of (3.2) by the following replacements:

$$\partial_x \rightarrow \partial_x + \epsilon^{1/2}\partial_X, \quad \partial_y \rightarrow \epsilon^{1/4}\partial_Y, \quad \text{and} \quad \partial_t \rightarrow \epsilon\partial_T, \tag{3.4}$$

where our control parameter ϵ is defined as

$$R = R_c + \epsilon R_c \ldots . \tag{3.5}$$

We also rewrite V as

$$V = \epsilon^{1/2} V_0 + \epsilon V_1 + \epsilon^{3/2} V_2 + \cdots . \tag{3.6}$$

The only new part of these calculations is to assume a three-mode solution:

$$V_0 = (A_1(X, Y, T)\mathrm{e}^{\mathrm{i}\boldsymbol{k}_1\cdot\boldsymbol{x}} + A_2(X, Y, T)\mathrm{e}^{\mathrm{i}\boldsymbol{k}_2\cdot\boldsymbol{x}} + A_3(X, Y, T)\mathrm{e}^{\mathrm{i}\boldsymbol{k}_3\cdot\boldsymbol{x}})\bar{\mathscr{V}}(z) + cc, \quad (3.7)$$

where

$$\bar{\mathscr{V}}(z) = \begin{bmatrix} \bar{\phi}(z) \\ \bar{\psi}(z) \\ \bar{\theta}(z) \end{bmatrix}. \quad (3.8)$$

The bar indicates that the z solutions have been minimized for marginal stability (see Scheel 2006). The variable $k = |k_1| = |k_2| = |k_3|$ is the critical wavenumber of the rolls, and A_1, A_2, A_3 are the amplitudes of the three modes, which are a function of X, Y and T only.

Note that the wave vectors have been chosen so that $\boldsymbol{k}_1 \cdot \boldsymbol{k}_2 = k^2 \cos\Theta_1$, $\boldsymbol{k}_2 \cdot \boldsymbol{k}_3 = k^2 \cos\Theta_2$ and $\boldsymbol{k}_1 \cdot \boldsymbol{k}_3 = k^2 \cos\Theta_3$, and $\Theta_1 + \Theta_2 + \Theta_3 = \pi$, where Θ_i is the smallest angle between A_i and A_j (remember that Θ is a director field so π maps onto 0).

To summarize, at order $\epsilon^{3/2}$, our multiple scales expansion and solvability condition lead to three coupled amplitude equations (for simplicity we will assume no spatial X, Y dependence):

$$\left.\begin{aligned} \tau_0 \partial_T A_1 &= A_1 - g_0|A_1|^2 A_1 - g_{12}|A_2|^2 A_1 - g_{13}|A_3|^2 A_1, \\ \tau_0 \partial_T A_2 &= A_2 - g_0|A_2|^2 A_2 - g_{21}|A_1|^2 A_2 - g_{23}|A_3|^2 A_2, \\ \tau_0 \partial_T A_3 &= A_3 - g_0|A_3|^2 A_3 - g_{32}|A_2|^2 A_3 - g_{31}|A_1|^2 A_3, \end{aligned}\right\} \quad (3.9)$$

where the coefficients τ_0, g_0 are found as a function of σ and Ω and are the same for each amplitude (Scheel 2007). The coefficients (g_{12}, g_{21}), (g_{13}, g_{31}) and (g_{23}, g_{32}) are also functions of σ and Ω as well as Θ_1, Θ_3 and Θ_2, respectively. Note that except for certain Θ_i values, $g_{ij} \neq g_{ji}$. The lateral boundary conditions are arbitrary at this point.

In all cases, we can solve for the steady state solutions A_{1s}, A_{2s}, A_{3s} as solutions to $\partial_T A_1 = \partial_T A_2 = \partial_T A_3 = 0$, respectively. The following solutions exist (Hoyle 2006):

(*a*) 1-mode ($A_{1s} = A_1$, $A_{2s} = A_{3s} = 0$),

(*b*) bimodal ($A_{1s} = A_1$, $A_{2s} = A_2$, $A_{3s} = 0$),

(*c*) trimodal ($A_{1s} = A_1$, $A_{2s} = A_2$, $A_{3s} = A_3$).

Note that squares are the special case that $A_1 = A_2$, $\Theta_1 = \pi/2$ and $g_{12} = g_{21}$. Also, hexagons are the case that $A_1 = A_2 = A_3$, $\Theta_1 = \Theta_2 = \Theta_3 = \pi/3$, $g_{12} = g_{31} = g_{23}$ and $g_{21} = g_{13} = g_{32}$.

We have plotted a few values of g_{ij} and g_{ji} as a function of Ω in figure 12(*a*). The quantity g_1 refers to the case where $i > j$, and the angle given is the angle between the rolls A_i and A_j. So g_1 can refer to either g_{12}, g_{13} or g_{23}. Likewise, g_2 refers to the case where $j > i$, or rotation in the opposite direction.

If a stationary solution exists, then we can solve for its stability against perturbations (Cross & Greenside 2009):

$$\left.\begin{aligned} A_{1p} &= A_1 + \delta A_1, \\ A_{2p} &= A_2 + \delta A_2, \\ A_{3p} &= A_3 + \delta A_3. \end{aligned}\right\} \quad (3.10)$$

We now rescale the time $T' = T/\tau_0$ and amplitudes $A_i' = \sqrt{A_i/g_0}$ and rotation coefficients $g_{ij}' = g_{ij}/g_0$ (and remove the primes).The perturbations are assumed to

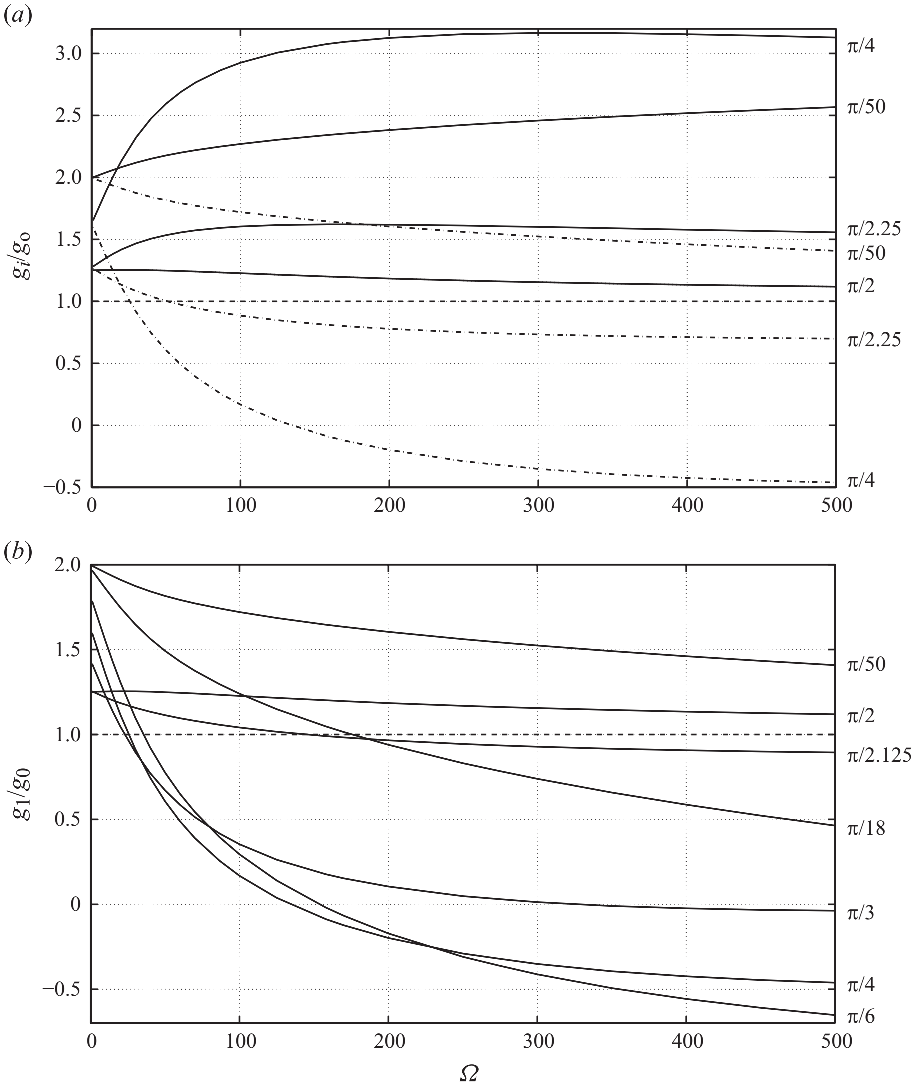

FIGURE 12. (*a*) A plot of g_1/g_0 versus Ω (dash-dotted lines) and g_2/g_0 versus Ω (solid lines) for various Θ values (as labelled) and for a Prandtl number of 6.4. (*b*) A plot of g_1/g_0 versus Ω for various Θ values (as labelled). Note that the line $g_i = g_0$ is drawn as a dashed line in both figures.

have the following growth rates:

$$\left.\begin{aligned} \delta A_1 &= \delta a_1 \mathrm{e}^{\sigma_1 T}, \\ \delta A_2 &= \delta a_2 \mathrm{e}^{\sigma_2 T}, \\ \delta A_3 &= \delta a_3 \mathrm{e}^{\sigma_3 T}. \end{aligned}\right\} \tag{3.11}$$

We solve for σ_1, σ_2 and σ_3 by substituting (3.11) into (3.9), linearizing in δa_i and then solving for the eigenvalues of the matrix equation

$$\begin{bmatrix} 1 - 3A_1^2 - g_{12}A_2^2 - g_{13}A_3^2 & -2g_{12}A_1A_2 & -2g_{13}A_1A_3 \\ -2g_{21}A_2A_1 & 1 - 3A_2^2 - g_{21}A_1^2 - g_{23}A_3^2 & -2g_{23}A_2A_3 \\ -2g_{31}A_3A_1 & -2g_{32}A_3A_2 & 1 - 3A_3^2 - g_{31}A_1^2 - g_{32}A_2^2 \end{bmatrix}. \tag{3.12}$$

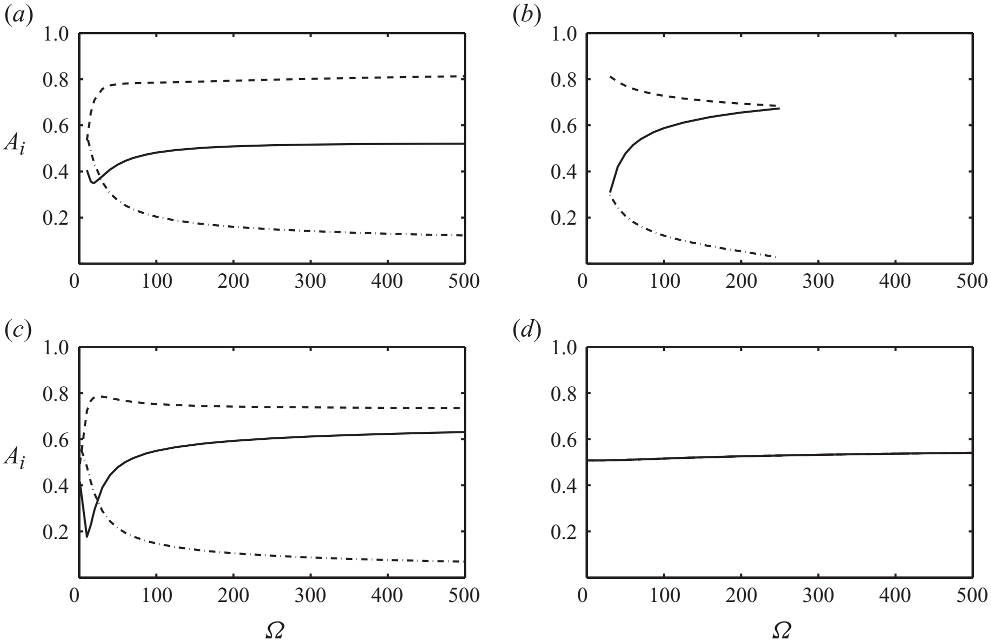

FIGURE 13. A plot of A_1 (solid line), A_2 (dash-dotted), A_3 (dashed) versus Ω for the coupled modes with angles (*a*) $(\pi/6, \pi/3, \pi/2)$, (*b*) $(\pi/3, \pi/6, \pi/2)$, (*c*) $(\pi/4, \pi/4, \pi/2)$, and (*d*) $(\pi/3, \pi/3, \pi/3)$. The amplitudes are plotted only for the cases where the stationary solutions exist.

Again, we can separate out our three cases to gain more insight.

(*a*) 1-mode: $|A_1| = 1$, $|A_2| = |A_3| = 0$, $\delta A_3 = 0$, $\sigma_1 = -2$, $\sigma_2 = 1 - g_{12}$. Straight, parallel rolls become unstable to rolls at an angle Θ_1 when $g_{12} < 1$. This is known as the Küppers–Lortz instability. As can be seen from figure 12(*b*), this first occurs at $\Omega = 23$ and $\Theta_1 = \pi/3$, consistent with prior results (Küppers & Lortz 1969). However, note that the band of unstable rolls widens rapidly as Ω increases. Also, the angle for the largest growth rate decreases as Ω increases. Note that for $\Omega = 200$ the maximum growth rate occurs at $\Theta = 33\pi/180$, exactly one of the switching angles seen in figure 1(*a*).

(*b*) Bimodal: $|A_1|^2 = (1 - g_{12})/(1 - g_{12}g_{21})$, $|A_2|^2 = (1 - g_{21})/(1 - g_{12}g_{21})$, $|A_3| = 0$. The bimodal state ceases to exist exactly at the Θ_1, Ω values for which the Küppers–Lortz instability sets in ($g_{12} < 1$). For Ω values less than this, the bimodal state is always unstable to the asymmetric state (one set of rolls growing and the other decaying). Also note that squares ($\Theta_1 = \pi/2$) always exist but are always unstable towards the asymmetric state. This positive growth rate for squares becoming unstable to the asymmetric state is plotted as a solid line in figure 14 as a function of Ω.

(*c*) Trimodal. In this case we solve for the eigenvalues of (3.12) for various possible combinations of Θ_1, Θ_2 and Θ_3 concurrently with the stationary solution to (3.9). We plot the stationary amplitudes (where they exist) in figure 13 and the real part of the growth rates in figure 14 for a few selected cases. Finally, we plot the imaginary part of the growth rates in figure 15.

The single and bimodal mode analysis agrees with the Küppers–Lortz results as expected. However, for the trimodal cases, there are Hopf bifurcations to modulated trimodal amplitude states, including the heteroclinic cycle ($\Theta_1 = \pi/3$, $\Theta_2 = \pi/3$,

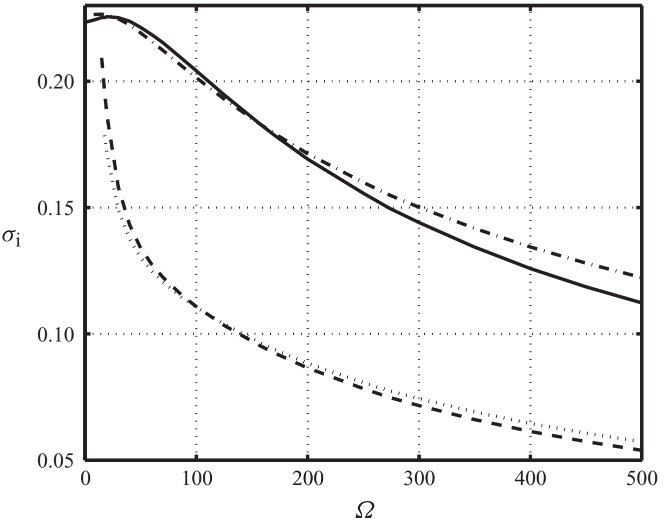

FIGURE 14. A plot of the real part of the positive growth rates σ_i versus Ω for coupled modes: the solid line denotes two coupled amplitudes ($|A_1| = |A_2|$, $\theta_1 = \pi/2$), growth rate associated with one mode growing and the other decaying. All the rest are for three coupled amplitudes, and the growth rate is complex and associated with an oscillatory mode: dashed line $= (\pi/6, \pi/3, \pi/2)$ and $(\pi/3, \pi/6, \pi/2)$, dotted line $= (\pi/4, \pi/4, \pi/2)$, and dash-dotted line $= (\pi/3, \pi/3, \pi/3)$.

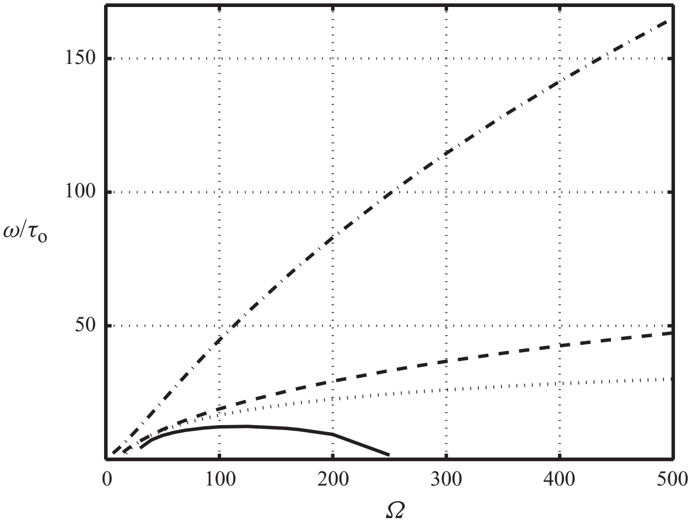

FIGURE 15. A plot of the imaginary part of the growth rates ω/τ_0 versus Ω for the three coupled oscillatory modes: dashed line $= (\pi/6, \pi/3, \pi/2)$, solid line $= (\pi/3, \pi/6, \pi/2)$, dotted line $= (\pi/4, \pi/4, \pi/2)$ and dash-dotted line $= (\pi/3, \pi/3, \pi/3)$. (Note that we divide by τ_0 to go from unscaled to scaled units).

$\Theta_3 = \pi/3$) as previously analysed (Goldstein *et al.* 1992). We have focused on the heteroclinic case as well as three other cases, $(\pi/6, \pi/3, \pi/2)$, $(\pi/3, \pi/6, \pi/2)$ and $(\pi/4, \pi/4, \pi/2)$. For high enough rotation rates, these three trimodal cases all exhibit a limit-cycle behaviour that is similar to the heteroclinic cycle, except that the amplitudes are unequal. We will focus on the $(\pi/6, \pi/3, \pi/2)$ case since it appears often in our simulations for our parameters, but the other ones have a similar behaviour. Since the mode amplitudes are unequal, and the amplitude for the $\pi/6$ roll set is much smaller than the other two, this trimodal oscillatory state can superficially resemble squares. Comparing figure 3 with figure 13(*a*) strongly suggests that this is the pattern seen at these rotation rates and near threshold. Note, however, that the agreement in amplitude could be better. Theoretically, we predict amplitudes of (0.81, 0.52, 0.12). Numerically, we find amplitudes of (0.78, 0.74, 0.16). Evidence supporting the MT state can also be seen by comparing the growth rates. The smallest positive growth rate in figure 14 is for $(\pi/6, \pi/3, \pi/2)$ at $\Omega = 200$, and the largest growth rate from rolls to tilted rolls in figure 12(*b*) is at about $\pi/6$ ($33\pi/180$ to be precise). Also, our oscillation frequency of rolls agrees best with the imaginary part of the growth rates for $(\pi/6, \pi/3, \pi/2)$ for all three rotation rates as seen in table 2. Note, however, that the oscillation frequency for $\Omega = 170$ is for a KL pattern and not an MT pattern. But, in general, the MT patterns have slightly higher frequencies than the KL frequencies, so this still supports the data.

4. Conclusion

In conclusion, for intermediate rotation rates and Prandtl numbers in rotating Rayleigh–Bénard convection, we find the existence of stable limit cycles consisting of three coupled oscillating amplitudes, both numerically and theoretically. Since one of the three amplitudes can be significantly smaller than the other two, these MT solutions can superficially resemble square patterns. Since square patterns are unstable in this parameter regime, these MT patterns provide a good explanation of the ‘square-like’ patterns seen in experiments and other simulations.

These MT solutions coexist with the KL solutions, hence it can be very difficult to end up with a pure MT solution. Sometimes the MT solutions are intermittent with KL states. This is particularly true when we start with random initial conditions. By starting with squares as the initial condition, we are more likely to see the MT pattern dominating.

Since many MT solutions exist for these parameters for a range of angles, as do a large band of KL states, it may be puzzling to understand why the $(\pi/6, \pi/3, \pi/2)$ MT state is selected in figure 1(*a*). However, for these parameters, the set of rolls with the largest growth rate is near $\pi/6$, so perhaps it is not so surprising that this roll angle is included in the MT state selected. In addition, the real part of the growth rate for the $(\pi/6, \pi/3, \pi/2)$ MT state is the smallest at $\Omega = 200$. Interestingly, the MT state seen in the $\Omega = 200$ case from figure 1(*a*) is incredibly stable. Multiple noisy restarts could not jostle it into a KL state. However, other cases, even simply starting from different initial conditions for $\Omega = 200$, led instead to mixed or intermittent MT/KL states. This is consistent with the results seen by Bajaj *et al.* (1998).

In addition, we find both numerically and theoretically that the MT patterns are independent of the inclusion of the centrifugal force, at least at low enough ϵ. However, to make an exact comparison with experiments, the centrifugal force needs to be included. As noted earlier, our Froude numbers are 0.03 and 0.07, which is in a regime where Marques *et al.* (2007) found quantitative and qualitative changes in the flow dynamics. Our results are in agreement with this claim.

Finally, we find no correlation between the wall mode and the bulk and conclude that these MT patterns are the result of a bulk instability for rotating Rayleigh–Bénard convection for this parameter regime.

The physical existence of trimodal patterns in rotating Rayleigh–Bénard convection may extend to other systems displaying similar symmetry. Also, more theoretical work should be done to better understand the stability and robustness of these patterns. For example, four-mode (or higher) amplitude equation solutions could also exist. We simply focused on three-mode solutions since those were most common for our parameters.

We thank Paul Fischer for the use of his numerical code Nek5000, which was used for the simulations and Guenter Ahlers and Michael Cross for insightful comments and helpful discussions. This work was supported by Jim and Sue Swenson. This research was supported in part by the National Science Foundation under grant PHY05-51164. The numerical code was run on the following supercomputing site, which we gratefully acknowledge: 'Jazz', a 350-node computing cluster operated by the Mathematics and Computer Science Division at Argonne National Laboratory as part of its Laboratory Computing Resource Center.

REFERENCES

Ahlers, G. & Bajaj, K. M. S. 1999 Rayleigh–Bénard convection with rotation at small Prandtl numbers. In *Pattern Formation in Continuous and Coupled Systems* (ed. M. Golubitsky, D. Luss & Steven H. Strogatz), *The IMA Volumes in Mathematics and its Applications*, vol. 115. Springer.

Bajaj, K. M. S., Lui, J., Naberhuis, B. & Ahlers, G. 1998 Square patterns in Rayleigh–Bénard convection with rotation about a vertical axis. *Phys. Rev. Lett.* **81**, 806–809.

Becker, N., Scheel, J. D., Cross, M. C. & Ahlers, G. 2006 Effect of the centrifugal force on domain chaos in Rayleigh–Bénard convection. *Phys. Rev.* E **73**, 066309.

Chang, Y., Liao, X. & Zhang, K. 2006 Convection in rotating annular channels heated from below. Part 2. Transitions from steady flow to turbulence. *Geophys. Astrophys. Fluid Dynamics* **100**, 215.

Chiam, K.-H., Paul, M. R., Cross, M. C. & Greenside, H. S. 2003 Mean flow and spiral defect chaos in Rayleigh–Bénard convection. *Phys. Rev.* E **67**, 056206.

Cross, M. C. & Greenside, H. 2009 *Pattern Formation and Dynamics in Nonequilibrium Systems*.

Demircan, A., Scheel, S. & Seehafer, N. 2000 Heteroclinic behavior in rotating Rayleigh–Bénard convection. *Eur. Phys. J.* B **13**, 765–775.

Demircan, A. & Seehafer, N. 2001 Nonlinear square patterns in Rayleigh–Bénard convection. *Europhys. Lett.* **53**, 202–208.

Fischer, P. F. 1997 An overlapping Schwarz method for spectral element solutions of the incompressible Navier–Stokes equations. *J. Comp. Phys.* **133**, 84–101.

Goldstein, H. F., Knobloch, E. & Silber, M. 1990 Planform selection in rotating convection. *Phys. Fluids* A **2**, 625.

Goldstein, H. F., Knobloch, E. & Silber, M. 1992 Planform selection in rotating convection: hexagonal symmetry. *Phys. Rev.* A **46**, 4755.

Hoyle, R. 2006 *Pattern Formation*. Cambridge University Press.

Hu, Y., Ecke, R. E. & Ahlers, G. 1995 Time and length scales in rotating Rayleigh–Bénard convection. *Phys. Rev. Lett.* **74**, 5040–5043.

Hu, Y., Ecke, R. E. & Ahlers, G. 1997 Convection under rotation for Prandtl numbers near 1: linear stability, wave-number selection and pattern dynamics. *Phys. Rev.* E **55**, 6928–6949.

Knobloch, E. 1998 Rotating convection: recent developments. *Intl J. Engng Sci.* **36**, 1421–1450.

Küppers, G. & Lortz, D. 1969 Transition from laminar convection to thermal turbulence in a rotating fluid layer. *J. Fluid Mech.* **35**, 609–620.

Marques, F. & Lopez, J. M. 2008 Influence of wall modes on the onset of bulk convection in a rotating cylinder. *Phys. Fluids* **20** 024109.

Marques, F., Mercader, I., Batiste, O. & Lopez, J. M. 2007 Centrifugal effects in rotating convection: axisymmetric states and three-dimensional instabilities. *J. Fluid Mech.* **580**, 303–318.

PAUL, M. R., CROSS, M. C & FISCHER, P. F. 2002 Rayleigh–Bénard convection with a radial ramp in plate separation. *Phys. Rev.* E **66**, 046210.

RUBIO, A, LOPEZ, J. M. & MARQUES, F. 2010 Onset of Kuppers–Lortz-like dynamics in finite rotating thermal convection. *J. Fluid Mech.* **644**, 337–357.

SÁNCHEZ-ÁLVAREZ, J. J., SERRE, E., CRESPO DEL ARCO, E. & BUSSE, F. H. 2005 Square patterns in rotating Rayleigh–Bénard convection. *Phys. Rev.* E **72**, 036307.

SCHEEL, J. 2006 Rotating Rayleigh–Bénard convection. PhD thesis, California Institute of Technology.

SCHEEL, J. D. 2007 The amplitude equation for rotating Rayleigh–Bénard convection. *Phys. Fluids* **19**, 104105.

SCHEEL, J. D. & CROSS, M. C. 2005 Scaling laws for rotating Rayleigh–Bénard convection. *Phys. Rev.* E **72**, 056315.

SCHEEL, J. D., PAUL, M. R., CROSS, M. C. & FISCHER, P. F. 2003 Traveling waves in rotating Rayleigh–Bénard convection: analysis of modes and mean flow. *Phys. Rev.* E **68**, 066216.

SCHLÜTER, A., LORTZ, D. & BUSSE, F. 1965 On the stability of steady finite amplitude convection. *J. Fluid Mech.* **23**, 129–144.

TU, Y. & CROSS, M C. 1992 Chaotic domain structure in rotating convection. *Phys. Rev. Lett.* **69**, 2515–2518.

ZHAN, X., LIAO, X., ZHU, R. & ZHANG, K. 2009 Convection in rotating annular channels heated from below. Part 3. Experimental boundary conditions. *Geophys. Astrophys. Fluid Dynamics* **103**, 443.

ZHANG, K. & LIAO, X 2008 The onset of convection in rotating circular cylinders with experimental boundary conditions. *J. Fluid Mech.* **622**, 63.